International Journal of Nanomedicine

Dovepress
open access to scientific and medical research

Open Access Full Text Article

ORIGINAL RESEARCH

A Chelate-Free Nano-Platform for Incorporation of Diagnostic and Therapeutic Isotopes

This article was published in the following Dove Press journal:
International Journal of Nanomedicine

Yaser H Gholami[1–4]
Lee Josephson[3]
Eman A Akam[5]
Peter Caravan[5]
Moses Q Wilks[3]
Xiang-Zuo Pan[3,6]
Richard Maschmeyer[1]
Aleksandra Kolnick[3,7]
Georges El Fakhri[3]
Marc D Normandin[3]
Zdenka Kuncic[1,4,8]
Hushan Yuan[3]

[1]The University of Sydney, Faculty of Science, School of Physics, Sydney, NSW, Australia; [2]Bill Walsh Translational Cancer Research Laboratory, The Kolling Institute, Northern Sydney Local Health District, Sydney, Australia; [3]Gordon Center for Medical Imaging, Department of Radiology, Massachusetts General Hospital, Harvard Medical School, Boston, MA, United States; [4]Sydney Vital Translational Cancer Research Centre, St Leonards, NSW, Australia; [5]The Institute for Innovation in Imaging and the A. A. Martinos Center for Biomedical Imaging, Department of Radiology, Massachusetts General Hospital, Harvard Medical School, Charlestown, MA, United States; [6]Bouve College of Health Sciences, CaNCURE Program, Northeastern University, Boston, MA, USA; [7]Internal Medicine Residency Program, Lahey Hospital and Medical Center, Burlington, MA, USA; [8]The University of Sydney Nano Institute, Sydney, NSW, Australia

Correspondence: Hushan Yuan
Gordon Center for Medical Imaging, Department of Radiology, Massachusetts General Hospital, Harvard Medical School, 149 13th Street, Charlestown, MA 02129, USA
Tel +1 617-643-1963
Email hyuan@mgh.harvard.edu

Purpose: Using our chelate-free, heat-induced radiolabeling (HIR) method, we show that a wide range of metals, including those with radioactive isotopologues used for diagnostic imaging and radionuclide therapy, bind to the Feraheme (FH) nanoparticle (NP), a drug approved for the treatment of iron anemia.

Material and methods: FH NPs were heated (120°C) with nonradioactive metals, the resulting metal-FH NPs were characterized by inductively coupled plasma mass spectrometry (ICP-MS), dynamic light scattering (DLS), and r_1 and r_2 relaxivities obtained by nuclear magnetic relaxation spectrometry (NMRS). In addition, the HIR method was performed with $[^{90}Y]Y^{3+}$, $[^{177}Lu]Lu^{3+}$, and $[^{64}Cu]Cu^{2+}$, the latter with an HIR technique optimized for this isotope. Optimization included modifying reaction time, temperature, and vortex technique. Radiochemical yield (RCY) and purity (RCP) were measured using size exclusion chromatography (SEC) and thin-layer chromatography (TLC).

Results: With ICP-MS, metals incorporated into FH at high efficiency were bismuth, indium, yttrium, lutetium, samarium, terbium and europium (>75% @ 120 °C). Incorporation occurred with a small (less than 20%) but statistically significant increases in size and the r_2 relaxivity. An improved HIR technique (faster heating rate and improved vortexing) was developed specifically for copper and used with the HIR technique and $[^{64}Cu]Cu^{2+}$. Using SEC and TLC analyses with $[^{90}Y]Y^{3+}$, $[^{177}Lu]Lu^{3+}$ and $[^{64}Cu]Cu^{2+}$, RCYs were greater than 85% and RCPs were greater than 95% in all cases.

Conclusion: The chelate-free HIR technique for binding metals to FH NPs has been extended to a range of metals with radioisotopes used in therapeutic and diagnostic applications. Cations with f-orbital electrons, more empty d-orbitals, larger radii, and higher positive charges achieved higher values of RCY and RCP in the HIR reaction. The ability to use a simple heating step to bind a wide range of metals to the FH NP, a widely available approved drug, may allow this NP to become a platform for obtaining radiolabeled nanoparticles in many settings.

Keywords: nanomedicine, radiolabeling, radionuclide therapy, HIR, Feraheme

Introduction

Radiolabeling methods yield nanomaterials used for the therapy and diagnosis of cancers[1–10] including for therapy of liver cancer (microspheres, arterial infusion),[11–15] and for sentinel lymph node delineation.[16–21] Here we examine a wide range of metals including many with radioactive isotopes used for diagnostic imaging or radionuclide therapy, for their ability to bind to the superparamagnetic iron oxide (SPION) nanoparticle (NP) known as Feraheme (FH), a drug approved for treating iron anemia and used off label as an MR contrast agent.[22–25] Using our chelate free,

heat-induced radiolabeling (HIR) method,[26–29] we show that this drug can be used as a broad nano-platform for radioisotope labeling.

Our radiolabeling method uses the Feraheme (FH), a NP with an iron oxide core (diameter ~5 nm) surrounded by a 10 nm thick polymeric coating (carboxymethyldextran, CMD), giving it an overall diameter of about 25 nm and a formula of Fe_{5874} O_{8752}:C_{11719} H_{18682} O_{9933} Na_{414} (See Figure 1A). Publications on the physical properties, pharmacokinetics (PK), toxicity and efficacy of FH as an MRI contrast agent provide knowledge regarding the likely behavior of radiolabeled FH in clinical settings, a body of knowledge unavailable with many other newly synthesized radiolabeled nanomaterials.

Current SPION radiolabeling methods fall into three classes. In the first class, a chelator is attached to a SPION by conjugation chemistry, followed by radiolabeling.[30–32] Storage of the chelator-modified SPIONs can be problematic

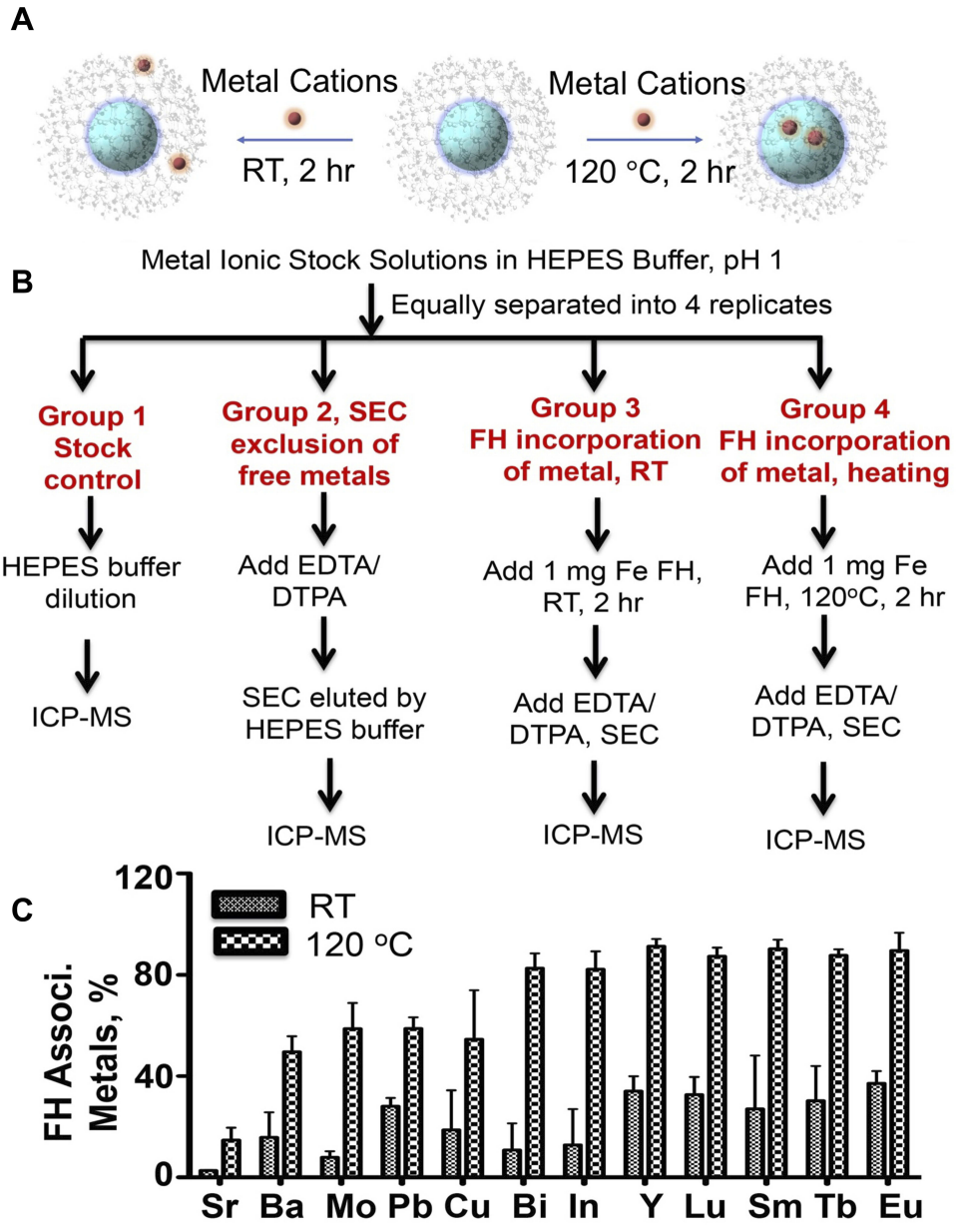

Figure 1 Summary of procedures used with HIR reactions. (**A**) A schematic diagram of the FH NP and its radiocation labeling at RT or 120°C is provided. The FH core iron oxide (blue) has a diameter of 5 nm while the polymeric coating is 10 nm thick, giving the NP an overall diameter of 17–31 nm. (Note: not to the exact scale.) (**B**) A flow chart summarizing procedures and conditions is provided. Size exclusion chromatography (SEC) separation was performed as indicated. (**C**) FH-associated metals at RT and 120°C analyzed by inductively coupled plasma mass spectrometry (ICP-MS).

due to the poisoning of the chelator by NP derived cations. In addition, the optimal chelator for in vivo stability can be different for different radiocations, and selecting a chelator can be a highly challenging task.[33–35] The second class of methods adds the radiocation during NP synthesis, so that the radiometal is incorporated throughout the metal oxide core.[36–39] This technique requires isotopes with long radiochemical half-lives compared to the time of synthesis and generates considerable volumes of low-level radioactive waste from washing the NP. The third class is the radiocation surface adsorption (RSA) methods. RSA methods allow cations to bind to the surface of a previously synthesized SPION.[40–42] With our HIR RSA method, heat is used to increase the bonding to the FH iron oxide[26–29] (see Figure 1A).

Previous HIR related studies used this technique to develop a diagnostic radiolabeled SPION using FH ($[^{89}Zr]Zr^{4+}$, $[^{64}Cu]Cu^{2+}$, $[^{111}In]In^{3+}$).[26–29] FH has been radiolabeled with zirconium-89 ($[^{89}Zr]$Zr-FH) and used to image monocyte infiltration as a way to assess inflammatory diseases since intravenously injected $[^{89}Zr]$Zr-FH showed enhanced uptake at the site of injury and in the draining lymph nodes.[29] HIR and surface click chemistry modification of FH also work cooperatively to provide a versatile nanoparticle platform for biomedical applications such as ex vivo cell labeling[27–29] and in vivo cell tracking including isolated B cells.[43]

An aim of this study was to investigate the HIR reaction for a range of therapeutic metals and to extend the use of the HIR radiolabeling technique for the development of a therapeutic/diagnostic FH platform (eg, $[^{90}Y]$Y-FH, $[^{177}Lu]$Lu-FH and $[^{64,67}Cu]$Cu-FH). A second aim was to further optimize the HIR technique to achieve higher radiochemical yield (RCY) for relatively short-lived isotopes (eg, copper-64). As far as we are aware, this study is the first attempt to radiolabel FH with $[^{90}Y]Y^{3+}$ and $[^{177}Lu]Lu^{3+}$. We anticipate the results of this work would facilitate the rapid development of chelate-free radiolabeling with diverse therapeutic/diagnostic metal isotopes with predictable and reliable specific activities.

Materials and Methods

The nonradioactive metal-FH HIR experiments were performed with 12 different nonradioactive cationic challenge metals of varying oxidation states, electron configurations, and atomic radii including Sr^{2+}, Ba^{2+}, Mo^{3+}, Pb^{2+}, Cu^{2+}, Bi^{3+}, In^{3+}, Y^{3+}, Lu^{3+}, Sm^{3+}, Tb^{3+}, and Eu^{3+}. Sr^{2+} and Ba^{2+} were used as substitutes for Ra isotope (all isotopes of radium are highly radioactive) and most of the others were directly corresponding to their therapeutic isotopic counterparts (see Table 1 and Figure 1A). In addition,

Table 1 ICP-MS Results (Average of Three Replicates) of: 1) Stock Concentrations of Metals for Reactions, 2) Low Molecular Weight Contamination of High Molecular Fraction, 3) Incorporation of Metals by FH Under Room Temperature (RT) and 120°C Heating, and 4) p-values

Metals	Concentrations of Reaction Metal Stocks in 2mL Volume (μm)*	**Low Molecular Weight Contamination of High molecular Fraction Contained by SEC, μM, (%)	***Concentration of FH Incorporated Metals at RT, μM (%)	***Concentration of FH Incorporated Metals at 120 °C, μM (%)	p–value****
	Column 1	Column 2	Column 3	Column 4	Column 5
Sr	22.7±1.59	0.02	0.62 ±0.05 (2.72 ±0.16%)	3.36±1.22 (14.70±4.91%)	p=0.0517
Ba	20.7±1.64	0.01	3.27±2.11 (15.75±9.90%)	10.23±1.11 (49.65±6.15%)	p=0.0115‡
Mo	35.4±2.83	0.24	2.77±0.72 (7.91±2.37%)	20.8±3.90 (58.83±10.13%)	p=0.0099‡
Pb	18.9±1.42	0.05	5.26±0.41 (28.06±3.29%)	11.14±1.64 (58.88±4.38%)	p=0.0009‡
Cu	14.1±3.49	0.01	2.81±2.30 (18.72±15.6%)	8.06±4.01 (54.62±19.31%)	p=0.0692
Bi	17.7±0.76	0.02	1.87±1.82 (10.78±10.56%)	14.64±1.60 (74.73±19.07%)	p=0.0016‡
in	20.8±0.61	0.01	2.62±2.90 (12.76±14.16%)	17.08±1.56 (78.06±4.99%)	p=0.0051‡
Y	19.1±1.05	0.01	6.52±1.4 (33.99±5.87%)	17.46±1.06 (91.31±2.85%)	p=0.0007‡
Lu	18.4±0.94	0.05	6.00±1.14 (32.58±7.03%)	16.04±1.20 (87.33±3.40%)	p=0.0014‡
Sm	20.3±0.35	0.04	5.46±4.29 (26.96±21.22%)	18.36±0.54 (90.28±3.63%)	p=0.0324‡
Tb	17.0±0.15	0.08	5.12±2.38 (30.16±13.90%)	14.89±0.24 (87.66±2.40%)	p=0.0157‡
Eu	17.7±0.33	0.03	6.54±0.77 (37.06±4.99%)	15.84±1.28 (89.64±6.95%)	p=0.0007‡

Notes: *Concentrations measured by ICP-MS analysis (1/10 of Stock solution B). **Concentrations (μM) of metals in larger molecular weight fraction (calibrated by FH) ***Concentrations (μM & %) of metals retained by FHNPs. ****Percentage (%) of doped metals at 120°C vs RT (Column 4 vs Column 3) by a one-tailed Welch's *T*-test. Significance (‡) was determined with FDR controls (α=0.05).

radioactive metal-FH HIR was performed with yttrium-90 and lutetium-177, as well as the shorter half-life isotope copper-64 to further improve the RCY of [^{64}Cu]Cu-FH.

Materials

The following metals were used as purchased: Indium (III) Chloride (Aldrich, ≥99.999% trace metal basis, 429,414), Samarium(III) chloride hexahydrate ($SmCl_3.6H_20$, Strem Chemicals, 93–6225), strontium chloride (Alfa Aesar, anhydrous, 99.5% metal basis, 16,790), copper(II) chloride ($CuCl_2$, Aldrich, 203,149-10G), yttrium(III) Chloride hydrate (Alfa Aesar, 99.99%, 11,185), bismuth(III) chloride (Alfa Aesar, anhydrous, 99.999%, 17,115), molybdenum(III) chloride (Alfa Aesar, anhydrous, 99.5% metal basis, 14,034), lutetium(III) chloride hexahydrate (Alfa Aesar, 99.9%, 11,260), lead(II) chloride (Alfa Aesar, 99.999% metal basis, 10,722), barium chloride (Alfa Aesar, anhydrous, 99.998% metal basis, 10,995), terbium (III) chloride hexahydrate ($TbCl_3.6H_20$, Acros Organics, 199,610,050), Europium(III) chloride hexahydrate, $EuCl_3.6H_20$, Acros Organics 193,010,050). HEPES was from Sigma Life Science (H7523-250G) and 0.5 M EDTA was from Invitrogen R1021. FH (30 mg Fe/mL) was purchased from the Massachusetts General Hospital Pharmacy and used without any further purification or modifications; the original vial contained 510 mg elemental iron per 17 mL (30 mg/mL). The following solvents were used as received Nitric Acid (Fluka, ≥69.0%, trace analysis grade), hydrochloric acid (Fluka, ≥37%, trace analysis). All aqueous solutions were prepared using Chelex 100 sodium form (Sigma) treated Millipore (18.2 $M\Omega.cm^{-1}$). The chelex-treated water (CTW, pH=10) was made as reported before.[29] Relaxation times were determined on a Bruker Mini SPEC MQ20, and particle sizes determined on a Malvern Instruments, ZetaSizer Nano Series, Nano-ZS.

In addition, [^{177}Lu]$LuCl_3$ solution was obtained from the radiochemistry research group at Royal North Shore Hospital (RNSH) with an activity concentration of 2 GBq/mL (1 GBq/0.5 mL, batch number: 139,179–012). [^{90}Y]YCl_3 solution was obtained from the radiochemistry research group at RNSH (Perkin Elmer/batch number C103116) with an activity concentration of 2.34 GBq/mL (3.29 GBq/1.41 mL). Also, [^{64}Cu]$CuCl_2$ was obtained from the South Australian Health and Medical Research Institute (batch number: 18-0218-902R) with an activity concentration of 2.93 GBq/mL (0.41 GBq/0.14 mL). 1 M and 25 mM Na_2CO_3 (Sigma-S7795-500G) were used for neutralization and pH adjustment of reaction mixtures. 20 mM and 10 mM of deferoxamine mesylate salt (DFO) (Sigma-D9533) were prepared and used to quench the reactions. For size exclusion chromatography (SEC), PD-10 columns (GE Healthcare) eluted with 0.9% saline were used. Volume fractions were counted on a Wizard 2480 (Perkin Elmer) gamma counter. Purified radiolabeled SPIONs were concentrated using an Amicon 30 kDa MC centrifugal filter (Sigma-Z717185). The TLC (Thin Layer Chromatography) plate used was a Strong Cation Exchange TLC plate made by Sorbent Technologies (Cat: 1224026). TLC plates were pre-soaked at the origin section by CTW and dried by a small fan immediately before use. The developed radio-TLC plates were divided into 1 cm pieces and the activity of each piece was measured using a Wizard 2480 (Perkin Elmer) gamma counter.

Synthesis of Nonradioactive Metal-FHs Using HIR Conditions

Generation of Stock Solutions

HEPES buffer (with pH 6–7, 0.1 M) was prepared by dissolving the HEPES salt in CTW under room temperature stirring for 24 hrs. Diluted NaOH was added to adjust the pH to 8–9. The concentrated stock solutions (called "Stock solution A") of Sr^{2+}, In^{3+}, Cu^{2+}, Y^{3+}, Lu^{3+}, Sm^{3+}, Tb^{3+}, Eu^{3+} and Bi^{3+}, were made by dissolving the metal chloride salts in 1 M hydrochloric acid. Because of their poor solubility, the stock solutions of Pb^{2+} and Mo^{3+} were made by dissolving the metal chloride salts into a mixture of 1 M hydrochloric acid: 70% nitric acid (v/v, 5:2). The reaction stock solutions (called "Stock solution B") (1 mL, between 140 and 350 μM, Table 1) were also made by diluting the concentrated stock solutions above (Stock solution A) with 0.1 M HEPES buffer. The pH was adjusted by adding concentrated HCl to pH 1, then each stock solution (Stock solution B) was identically separated into 4 groups (200 μL/group, details of Groups 1–4: see flow chart in Figure 1B) and the reactions and ICP-MS analysis (Figure 1C) were performed as per following:

Procedure for PD-10 SEC Fraction Collection

The PD-10 column was calibrated by FH NPs as the larger molecular marker and vitamin B_{12} as the small molecular marker. The dead volume for separating the FH NPs from small molecular contaminants (eg, metal chelated DFO) was 2.5 mL. The FH NP fraction was the next 1.8 mL from 2.5 to 4.3 mL and the vitamin B_{12} fraction was the next 6 mL from 4.3 to 10.0 mL. All the metal sample

solutions (Group 2–4, Table 1 and Figure 1B) were loaded onto the 0.1 M HEPES buffer preconditioned PD-10 columns and eluted by the same buffer. The fractions from 2.5 to 4.3 mL were collected. After a final volume (2 mL) was made by adding 0.1 M HEPES buffer (200 µL), the sample solutions were applied to ICP-MS digestion and analysis (ICP-MS procedure, see below).

Sample Preparation of Groups 1–4 (Table 1, Figure 1B)

Group 1: for ion concentration confirmation: the 200 µL metal solutions (Stock solution B, 140 −350 µM, Column 1 of Table 1) were further diluted into 2 mL by 0.1 M HEPES buffer. After the addition of trace amount of concentrated HCl to pH 1, the solutions were sent to ICP-MS digestions and analysis (Column 1 of Table 1). The concentrations of nonradioactive metals used in this study were around 200 µM (Table 1), which were about 20 times higher than the $[^{89}Zr]Zr^{4+}$ concentration of the higher activity of zirconium-89 (A_0=370 MBq/mg, [Zr] ≈ 9 µM) that was used in the previous [^{89}Zr]Zr-FH HIR study.[29]

Group 2: for PD-10 column size exclusion chromatographic (SEC) separation confirmation (ICP-MS cation concentrations: see Column 2 of Table 1): to the 200 µL metal solutions (Stock solution B), were added NaOH (20 M) to adjust pH to 7–8, then 8 µL of 0.5 M EDTA and 8 µL of 0.5 M DTPA chelators were added. After incubation at room temperature for 15 min, the mixtures were loaded onto PD-10 columns, respectively, eluted by 0.1 M HEPES buffer, and fraction collected as above.

Group 3: for FH incorporation of cations at room temperature (RT) (ICP-MS cation concentrations: see Column 3 of Table 1): to the 200 µL metal solutions (Stock solution B) (pre-adjusted to pH 7–8 as Group 2) in a 5 mL glass v-vial fitted with magnetic stir bar, FH (1 mg Fe, 33.3 µL) and 0.1 M HEPES (66.7 µL) were added. The final pH was adjusted to 8–9 by adding 2 M NaOH solutions. The reaction mixtures were stirred and incubated under RT for 2 hrs. After 8 µL of 0.5 M EDTA and 8 µL of 0.5 M DTPA were added and incubated at RT for 15 mins, the mixtures were loaded onto PD-10 columns, respectively, eluted by 0.1 M HEPES buffer, and fraction collected as above.

Group 4: for FH incorporation of cations at 120°C (HIR condition, ICP-MS cation concentrations: see Column 4 of Table 1): to the 200 µL metal solutions (Stock solution B) (pre-adjusted to pH 7–8 as Group 2) in a 5 mL glass v-vial fitted with magnetic stir bar, FH (1 mg Fe, 33.3 µL) and 0.1 M HEPES (66.7 µL) were added. The final pH was adjusted to 8–9 by adding 2 M NaOH solutions. The reaction mixtures were stirred and incubated under 120°C for 2 hrs. Then, the vial was cooled down to room temperature in an ice-water bath for 15 min. Next, 8 µL of 0.5 M EDTA and 8 µL of 0.5 M DTPA were added and incubated at room temperature for 15 min. Afterward, they were loaded onto PD-10 columns, respectively, eluted by 0.1 M HEPES buffer, and fraction collected as above.

Pre-Treatments of ICP-MS Samples and ICP-MS Analyses

The measurements for the concentrations of metal cations were carried out using an Agilent 8800-QQQ Inductively Coupled Plasma Mass Spectrometer (ICP-MS) system. Calibration curves were generated from commercially available standards (Sigma-Aldrich and Aristar). Metal containing solutions (Group 1 – Group 4, Figure 1B) were weighted (around 0.1000 g/each sample) into 15 mL Falcon tubes. To the tubes were added ICP compatible matrix containing TritonX and nitric acid per manufacturer's instructions (around 4.000 g/each sample). The samples were digested at 37°C overnight prior to analysis. The ICP-MS results were presented in Tables 1 and 2 and figuratively displayed in Figures 1C, 2A and B.

Size and Relaxivity Measurements of Non-Radioactive HIR Metal-FH

A solution of nonradioactive HIR metal-FH with 0.9 mM Fe was made in 0.1 M HEPES buffer for each sample. The sizes (Table 2, Figure 2C) were measured by a Malvern Instruments, ZetaSizer Nano Series, Nano-ZS. The solutions of nonradioactive HIR metal-FH were made in three concentrations of Fe (0.9 mM, 0.3 mM, and 0.1 mM) for each sample. The relaxivities (r_1 and r_2, Table 2 and Figure 2D) were determined in 0.1 M HEPES buffer. FH treated under the same HIR heating condition was the references for both size and relaxivity measurements.

Statistical Analyses

Statistical analyses have been made for Figures 1C and 2A–D, including:

Metal Association Due to Heating (for Figure 1C)

The increase in metal association between room temperature and heated incubation was tested for each metal. The increase in association was tested using Welch's *T*-test with false discovery rate (FDR) controls.

Table 2 Characterization of Nonradioactive Metal-FH NPs: Metals Retained by FH NPs (%) Before and After Buffer Wash, Sizes, and Relaxivities (r_1, r_2)

FH NPs	Metal Retained by FH NPs Doped at RT With or Without Wash (%)*		Metal Retained by FH NPs Doped at 120 °C With or Without Wash (%)*		Sizes (d, nm)** (p-Value)	Relaxivity ($s^{-1}.mM^{-1}$) r_1, (p-value) r_2, (p-value) ***
	Without Wash	With Wash	Without Wash	With Wash		
Sr	2.73	1.65	16.83	14.98	28.65±1.43 (p=8.19E-06 [†])	35.16±1.130 (p=0.08591) 82.64±2.58 (p=0.0004347[†])
Ba	22.2	20.43	43.48	43.27	28.04±1.38 (p=9.57E-06 [†])	35.47±2.209 (p=0.1895) *87.66±5.34* (p=0.000248[†])
Mo	8.19	3.93	50.97	46.74	27.49±1.56 (p=4.59E-05[†])	33.75±0.67 (p=0.002184 [†]) 75.81±1.60 (p=0.02839)
Pb	30.34	11.70	53.91	32.41	28.95±2.06 (p=1.11E-04[†])	34.48±4.060 (p=0.4315) 84.39±1.00 (p=0.0001[†])
Cu	17.28	4.15	61.86	38.69	31.00±2.14 (p=4.04E-05[†])	36.63±2.050 (p=0.7984) 90.06±5.09 (*p=0.0001*[†])
Bi	22.45	8.37	76.48	52.92	27.35±0.73 (p=1.82E-08[†])	34.48±4.06 (p=0.1678) 84.39±1.00 (p=0.0001[†])
in	5.81	2.42	88.41	75.95	32.13±0.86 (p=1.06E-09[†])	34.44±0.59 (p=0.01202) 84.39±1.00 (p=0.0001[†])
Y	40.49	17.69	89.12	73.38	27.15±0.77 (p=4.51E-08[†])	36.37±2.930 (p=0.8109) 90.82±7.54 (p=0.0004524[†])
Lu	39.61	18.64	84.17	71.83	26.70±0.45 (p=7.80E-09)	37.76±4.840 (p=0.7011) 91.46±6.49 (p=0.0001[†])
Sm	39.76	16.81	86.66	71.47	27.07±1.66 (p=1.10E-04)	33.21±0.13, (p=0.000335[†]) 76.51±0.69 (p=0.01964[†])
Tb	39.87	17.79	85.97	74.47	27.18±0.80 (p=6.24E-08)	34.48±4.060 (p=0.8841) 84.39±1.00 (p=0.003752[†])
Eu	42.81	20.78	85.28	73.38	27.37±0.51 (p=2.39E-09)	36.92±3.380 (p=0.6321) 83.38±9.89 (p=0.1546)
FH					20.88±0.59	37.63±0.670 77.69±0.25

Notes: *Paired Test on percent retained, with vs without heating; p-value = 2.53E-07; average retrained at RT: 47.36%; average retrained heating: 81.74%. **Two-tailed Welch's *t*-test, significance ([†]) was determined with FDR controls (α = 0.05), mean increase of 7.38nm after metal addition. ***ANCOVA fitting for r1 and r2 was done for all compounds between each metal and the base FH. Significance ([†]) was determined with FDR controls (α = 0.05).

Metal Retention After Washing (for Figure 2A and B)

The effects of heating vs room temperature on metal retention after washing were tested using a paired *T*-Test. The percent of labeled metal retained after filtering was compared between heating and room temperature incubation for each metal.

Size (for Figure 2C)

The sizes of all metal-FHs were compared to the size of un-doped Feraheme using a two-tailed Welch's *T*-Test, with FDR controls.

Relaxivities (for Figure 2D)

For each metal-FH, the slopes of the resultant relaxivity curves were compared to those of the unmodified FH NPs using ANCOVA analysis with FDR controls.

Synthesis of Radioactive Metal-FHs Using HIR Conditions

The HIR procedure was described in previous studies.[29] Some modifications such as heating vortex (HV) mixing (Figure S1), temperature elevation, and shortened reaction time were made to the HIR technique to further optimize radiolabeling of FH with the therapeutic ($^{9Y}Y^{3+}$ and [^{177}Lu]Lu^{3+}) and relatively short half-life ([^{64}Cu]Cu^{2+}) isotopes. Similar SEC purification steps to the nonradioactive metal-FH were utilized for the [^{177}Lu]Lu-FH, [^{90}Y]Y-FH and [^{64}Cu]Cu-FH syntheses. All of the radiochemical analysis results were decay corrected. In addition, the radiochemical yield (RCY) and purity (RCP) of radiolabeled FH (radio-FH) products were obtained by the division of the activity of the radio-FH by the amount of activity used at the beginning.[29]

[^{90}Y]Y-FH Radiolabeling

After dilution of the original [^{90}Y]YCl_3 in HCl (0.1 M), two identical samples were prepared. For each sample, the reaction mixture was prepared by adding [^{90}Y]YCl_3 (38 µL, $A_0 \approx 30$ MBq, $m_Y \approx 0.0166$ nmoles, $N_{Y,atoms} \approx 10^{13}$) and CTW (50 µL) into a 0.3 mL glass vial. The pH of the reaction mixture was adjusted to 8–9 by adding Na_2CO_3 (40 µL, 1 M in CTW) gradually. FH (33.3 µL, 1 mg Fe) was added to the reaction mixture and the total volume was brought up to 250 µL by adding CTW (88.7 µL). The final pH of the reaction mixture was reassured to be 8–9 (Supplementary Figure S1a and b). The glass vial was placed in a heating vortex silicon oil bath (Supplementary Figure S1c and d) and the reaction mixture was heated for 2 hrs at 120–130°C under vortexing. The reaction mixture was cooled down in an ice bath for 15 min under vortexing. DFO (5 µL, pH 7.5, 20 mM in CTW) was added to quench the reaction by reacting with any remaining free [^{90}Y]Y^{3+} and dissociating loosely bound [^{90}Y]Y^{3+} ions from FH. A PD-10 column was used for the SEC purification and the fraction collection was done as

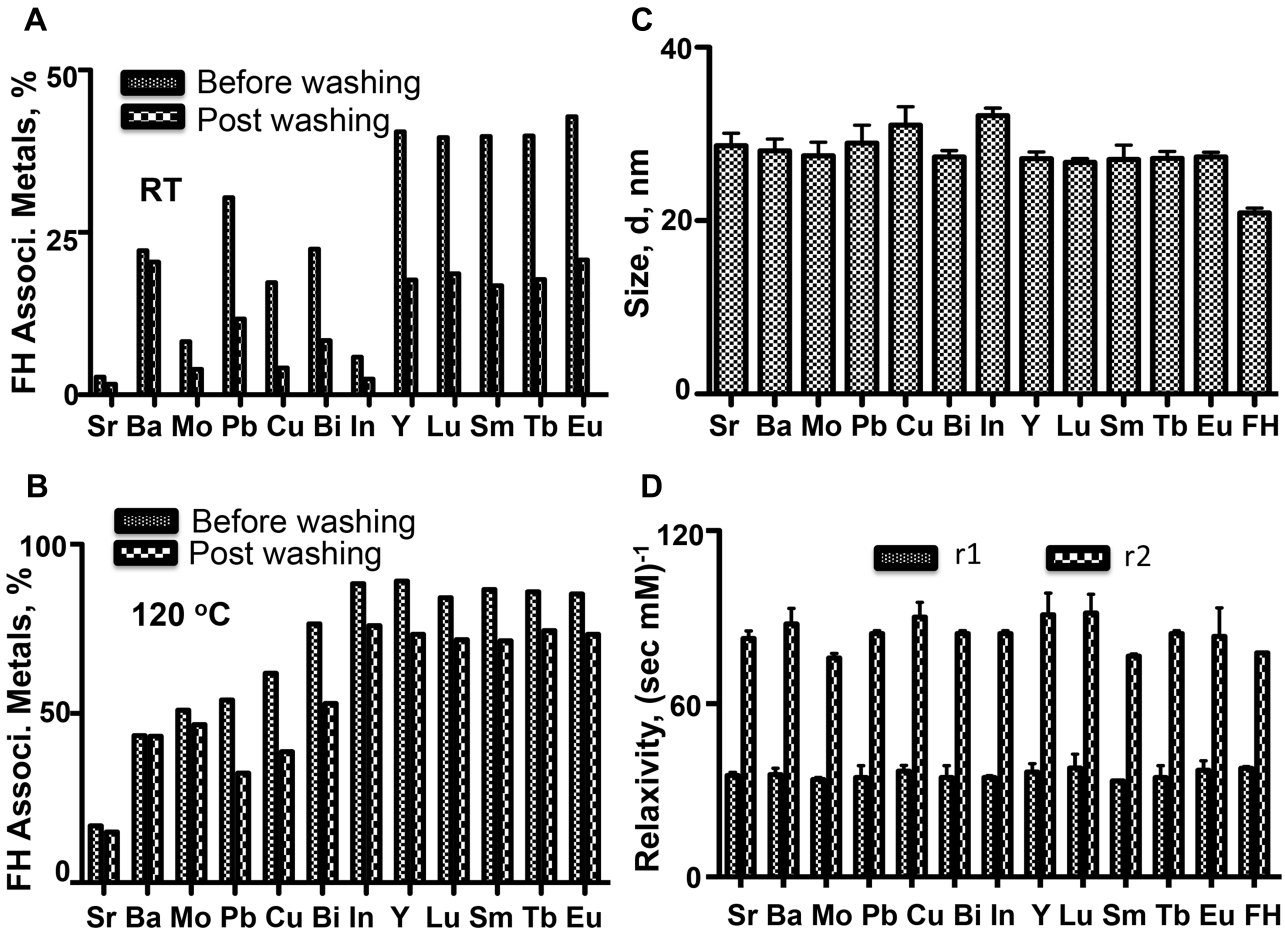

Figure 2 Characterization of metal-doped FHs. (**A**) RT reaction for FH-associated cations obtained before and after washing with 0.1 M HEPES and separation of the wash with Amicon filters. (**B**) 120°C reaction for FH-associated cations obtained as in 2a. (**C**) Sizes (diameter, nm) of metal-doped FHs obtained by light scattering. (**D**) Transverse (r_1, spin-lattice) and longitudinal (r_2, spin-spin) relaxivities of metal-doped FHs and the control FH are shown.

above for Groups 3 and 4 for nonradioactive metal-FH (Supplementary Figure S2a–d). The purified product was concentrated by centrifugation with a 50 kDa MC Amicon filter at 370 g (rcf) under room temperature (Supplementary Figure S3a–d). The final purified product was then collected in saline at 200 µL with approximately complete recovery (Supplementary Figure S3e). Finally, SEC analysis was performed for the purified product to calculate the RCP (Table 3) (procedure see below).

[^{177}Lu]Lu-FH Radiolabeling

After dilution of the original [^{177}Lu]$LuCl_3$ in HCl (0.1 M), two identical samples were prepared. For each sample, firstly the reaction mixture was prepared by adding [^{177}Lu]$LuCl_3$ (20 µL, $A_0 \approx 15$ MBq, $m_{Lu} \approx 0.0206$ nmoles, $N_{Lu,atoms} \approx 1.2 \times 10^{13}$) and CTW (50 µL) into a 0.3 mL glass vial (see Supplementary Figure S1e, f). The pH of the reaction mixture was adjusted to 8–9 by adding Na_2CO_3 (20 µL, 1 M in CTW) gradually. FH (33.3 µL, 1 mg Fe) was added to the

Table 3 A Summary of Measured Decay Corrected RCY and RCP for Radiolabelled-FH Products*

HIR-FH	Temperature	Reaction Time	RCY	RCP
[^{90}Y]Y-FH, n=5	140°C	2 hr	94.0 ± 0.8% (HIR)	97.5 ± 1.0%
[^{177}Lu]Lu-FH, n=3	140°C	2 hr	91.0 ± 0.7% (HIR)	95.0 ± 0.7%
[^{64}Cu]Cu-FH, n=3	140°C	1 hr	87.2 ± 1.2% (HV-HRR-HIR)	99.0 ± 1.2%
[^{64}Cu]Cu-FH, n=3	140°C	1 hr	76.6 ± 1.1% (HRR-HIR)	98.5 ± 1.1%
[^{64}Cu]Cu-FH, n=3	120°C	2 hr	68.0 ± 1.1% (HIR)	98.5 ± 1.2%

Note: *Average of five replicates for [^{90}Y]Y-FH and three replicates for both [^{177}Lu]Lu-FH and [^{64}Cu]Cu-FH.

reaction mixture and the total volume was brought up to 200 µL by adding CTW (96.7 µL). The final pH of the reaction mixture was reassured to be 8–9. The glass vial was placed in a heating vortex silicon oil bath and the reaction mixture was heated for 1 hr at 120–130°C under vortexing. The reaction mixture was cooled down in an ice bath for 15 mins under vortexing. DFO (5 µL, pH 7.5, 20 mM in CTW) was added to quench the reaction by reacting with any remaining free radioactive [^{177}Lu]Lu^{3+} and dissociating the loosely bound [^{177}Lu]Lu^{3+} ions from FH. A PD-10 column was used for the SEC purification and collected as above for Groups 3 and 4 for nonradioactive metal-FH. The purified product was concentrated by centrifugation with a 50 kDa MC Amicon filter for 370 g (rcf) under room temperature (Supplementary Figure S3a–d). The final purified product was then collected at 200 µL with approximately complete recovery (Supplementary Figure S3e). Finally, SEC analysis was performed for the purified product to calculate the RCP (Table 3) (procedure see below).

[^{64}Cu]Cu-FH Radiolabeling

Three reaction mixtures were prepared for optimization of HIR conditions for higher Specific Activity (A_s) [^{64}Cu]Cu-FH syntheses. In general, the procedures were very similar to that for HIR syntheses of [^{177}Lu]Lu-FH and [^{90}Y]Y-FH except the variations indicated below including the amount of activities, temperature, reaction time, and stirring methods (Table 3).

For HIR [^{64}Cu]Cu-FH Radiolabeling

Two samples with A_0 = 18 MBq and 1 mg Fe FH were prepared using similar procedures for [^{90}Y]Y-FH and [^{177}Lu]Lu-FH described above with heating temperature at 120°C for 2 hrs under magnetic stirring (Table 3).

For Higher Reaction Rate HIR (HRR-HIR)

Higher reaction rate was achieved by increasing the initial activity to A_0 = 22 MBq of [^{64}Cu]$CuCl_2$, reacting at an elevated temperature at 140°C, and shortening the reaction time to 1 hr under magnetic stirring (Table 3). The reaction rate $\dot{R}(t)$ for HRR-HIR and HIR was estimated using the cumulative activity equation[44] (1):

$$\dot{R}(t) = \frac{\tilde{A}\int_0^T e^{-\lambda t}dt}{T} = \frac{\frac{A_0}{\ln(0.5)} \times t_{1/2}\int_0^T e^{-\ln(0.5)\frac{t}{t_{1/2}}}dt}{T} \quad (1)$$

where $\tilde{A}$, A_0, T and $t_{1/2}$ are the cumulative activity, the initial activity, the reaction time and the isotope half-life. The reaction rate calculations are exemplified in Supplement Materials.

For Higher Reaction Rate HIR Under Heating Vortex (HRR-HV-HIR)

The third set of [^{64}Cu]Cu-FH reaction mixture was prepared similar to HRR-HIR technique, except that the heating vortex (HV) technique (Figure S1) was used instead of magnetic stirrer for mixing the reaction mixture during the reaction (Table 3).

Measurements for RCY and RCP

For both RCY and RCP analyses were performed using SEC and TLC methods. The SEC for RCY and RCP analyses recruited reported procedures.[29] For both [^{177}Lu]Lu-FH and [^{64}Cu]Cu-FH, the activity was counted by a gamma-counter, and decay-corrected elution curves were plotted for [^{177}Lu]Lu-FH (see Figure 3A, B and E, F) and [^{64}Cu]Cu-FH (see Figure 3C, D and G, H). For the analysis of [^{90}Y]Y-FH, a bremsstrahlung-based technique[45] had to be developed as [^{90}Y]Y is not a direct gamma emitter, and thus the conventional gamma-counter method cannot be used. The gamma-counter protocol was modified by setting the energy window to 2–2000 keV to detect the produced secondary bremsstrahlung radiation emitted by the beta particles. Then, the [^{90}Y]Y-FH SEC and TLC chromatogram were plotted (Figure 3A, B and E, F). In addition, to validate this technique the bremsstrahlung counts corresponding to 30 MBq [^{90}Y]YCl_3 (five replicates and the average value was used as the reference) and the activity of [^{90}Y]Y-FH product was measured and their ratio was compared against the ratio of the areas under the SEC and TLC chromatograms of [^{90}Y]Y-FH and [^{90}Y]Y-DFO. The ratio of area of [^{90}Y]Y-FH and [^{90}Y]Y-DFO under the curves also represents the RCY measured by a dose calibrator (ie, the ratio of [^{90}Y]Y-FH and [^{90}Y]YCl_3 activities) and thus the ratio of the bremsstrahlung counts corresponding to the [^{90}Y]Y-FH and [^{90}Y]YCl_3 activities should agree with the RCY measurements to validate the bremsstrahlung counts technique.

Results

Nonradioactive Metal-FHs

SEC Exclusion of Free Nonradioactive Metals by PD-10 Columns

It was critical to validate whether a simple SEC procedure by a PD-10 column could completely eliminate the free metal cations. The ICP-MS analyses indicated that all the samples in Group 2 had less than 1% metal contamination at larger molecular fractions (Column 2 of Table 1). This proved that a PD-10 SEC procedure could be sufficient to remove all the free metals at this scale.

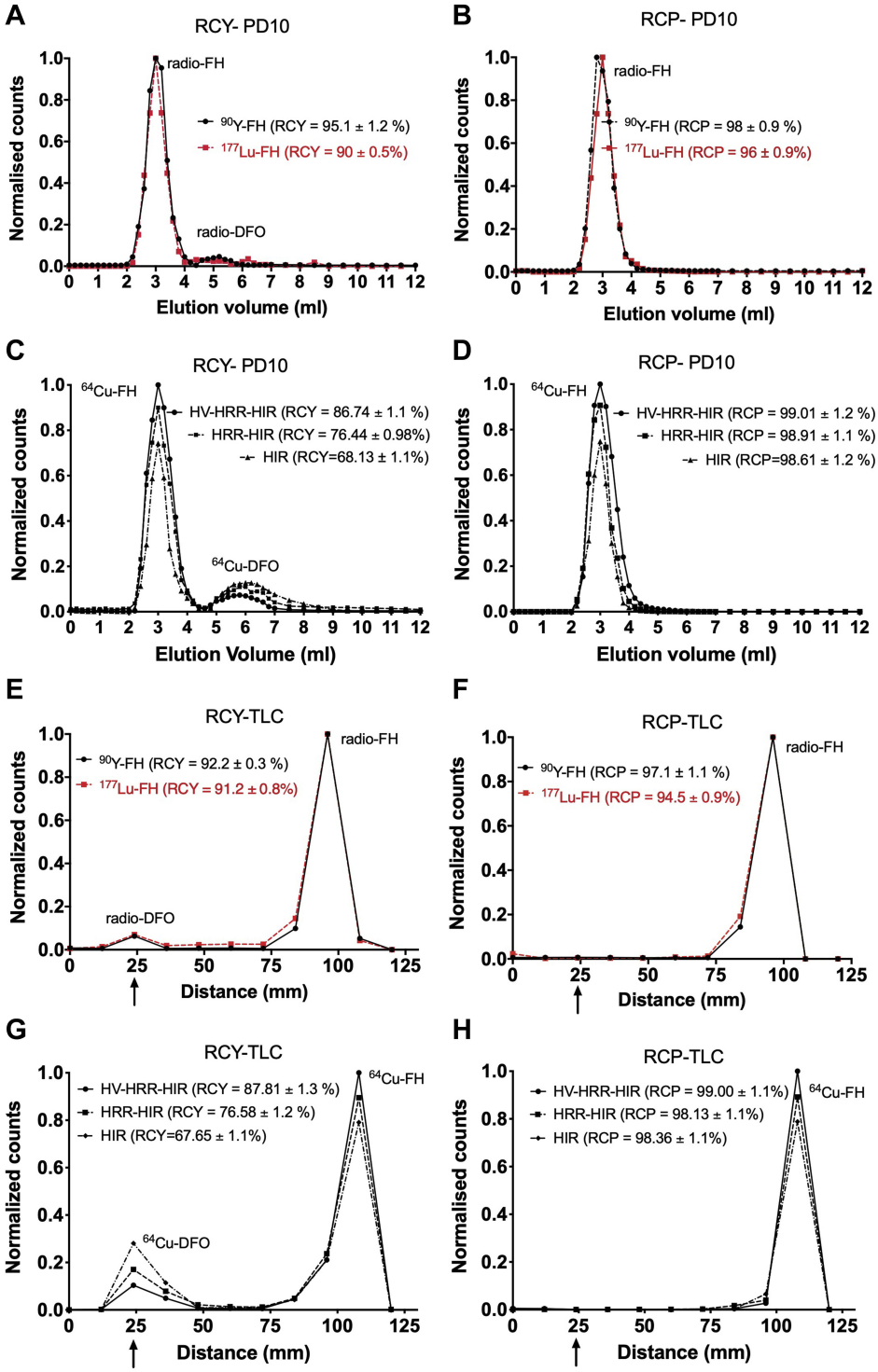

Figure 3 Characterization of crude reaction mixes and purified products for HIR-FH labeled with different radiocations. (**A**) The radiochemical yields (RCY) by SEC (PD-10 column) for reaction mixes yielding [^{90}Y]Y-FH or [^{177}Lu]Lu-FH are shown. Deferoxamine (DFO) is added to remove loosely bound radiocations from FH, and to ensure that radiocations are not present as oxides, but as low molecular weight, radio-DFO complexes. These complexes migrate at the included column volume in SEC or stay at the origin in TLC. See legend for 3e below. All values are decay corrected. Integrated areas under the peaks were used to obtain RCY or RCP. (**B**) Radiochemical purity (RCP) by SEC after reaction mixes from (**A**) was purified by SEC. (**C**) RCY by SEC for reactions yielding [^{64}Cu]Cu-FH is shown. Because the RCY for [^{64}Cu]Cu-FH (68.1%) was lower than that seen with [^{90}Y]Y-FH or [^{177}Lu]Lu-FH (90.1% or 95.1% in Figure 3a), variants of the standard HIR procedure, the HRR-HIR and HV-HRR-HIR procedures, were developed. (**D**) RCP by SEC after reaction mixes from (**C**) was purified by SEC. (**E**) RCY by TLC for reaction mixes yielding [^{90}Y]Y-FH or [^{177}Lu]Lu-FH is shown. With TLC, radio-DFO complexes remain at the origin (arrows) while negatively charged radio-FH NPs move to the solvent front on our negative charged, cation exchange TLC plates. (**F**) RCP by TLC after reaction mixes from (**E**) was purified by SEC. (**G**) RCY by TLC for reactions yielding ^{64Cu}Cu-FH. (**H**) RCP by TLC after reaction mixes from (**G**) was purified by SEC.

Incorporation of Nonradioactive Metal Cations

Incorporation of nonradioactive metal cations was carried out by incubating the FH and cation mixtures under both RT and heating (120°C, HIR heating condition) for 2 hrs. The collected FH fractions were analyzed by ICP-MS and the data are listed in Table 1 (RT: see Column 3; 120°C heating: see Column 4) and plotted by bar graph in Figure 1C. At RT, less than 20% incorporation of Sr, Ba, Mo, Bi, Cu, Bi, and In was found. Pb, Y, Lu, Sm, Tb, and Eu, however, had 28-37% eluted together with FH. This incorporation is likely due to the FH NP's CMD coating which contains multivalent carboxyl groups capable of metal binding. Carrying out metal incorporations onto FH at 120°C resulted in an overall increase of incorporation for all elements (Figure 1C). The extent of metal incorporation varied depending on the element. For s-block elements, Sr had the lowest incorporation among all the studied metals with ~15% incorporation. Ba residing in the same group as Sr, however, had a 3-fold increase to ~50%. The p-block Pb and d-block Cu and Mo demonstrated similar binding efficiency of ~55%–59%. Although we cannot fully explain why Mo^{3+} had similar binding efficiency, the lower efficiency for Pb and Cu may be attributed to their lower charge densities resulting in a weaker charge associated binding to the negative iron oxide core $[Fe\text{-}O]^{-}$. In contrast, trivalent p-block (Bi^{3+}, In^{3+}), d-block (Y^{3+}), and f-block (Lu^{3+}, Sm^{3+}, Tb^{3+}, and Eu^{3+}) metals displayed the highest binding efficiency ~75% - 91%. These ions are more likely to interact with other electron donors such as the oxygens on the surface of iron oxide core.[46] The statistical analysis indicated that all metals except for Cu and Sr showed significantly increased association due to heating, with a mean 4-fold increase. The remaining metals, Cu (p=0.0692) and Sr (p=0.0517), did not show significant increases.

Characterization of Nonradioactive Metal-FH NPs

The stability of metals incorporated with FH was assessed by a washing method. We hypothesized that loosely bound metals would pass through the 50 kDa filter during the centrifugation, while the HIR tightly bound metals shall be retained by the FH NPs. The SEC purified metal-FH NP (600 µL) was transferred into a 50k Da molecular cutoff Amicon filter and centrifuged under 5000g rcf at 4°C until the volume reduced down to 100 µL. Then, the concentrated metal-FH NPs were washed by 0.1 M HEPES buffer (2 × 300 µL). The washed samples were analyzed by ICP-MS and the cation concentrations are given in Table 2 and shown in Figure 2A and B. Except Ba with only 8% loss, more than half of the metals (51.5% - 76.0%) washed off the FH NPs doped at RT. However, except Cu^{2+} with 37.5% of loss, Pb^{2+} with 40.0% loss, and Bi with 30.8% loss, other metal-FH NPs doped at 120°C had less than 18% loss. In fact, paired T-tests show that heating significantly increased metal retention after filtering (81.74%) than room temperature incubation (47.36%) (p=2.53E-07). This is a solid evidence of the tight binding of metals when doped under 120°C (HIR) conditions.

In addition to the stability of doped metals, the particle sizes (Table 2 and Figure 2C) and relaxivities (r_1 and r_2, Table 2 and Figure 2D) were also measured to characterize the HIR metal-FH NPs. A small but significant size increase (7.38 nm mean increase in diameter) was found for HIR metal-FH NPs comparing with FH NPs treated under the same condition without metals. However, the sizes are still in the reported range of FH NPs (20–33 nm in diameter).[47–49] The relaxivity measurements (Table 2 and Figure 2D) indicate that r_1 and r_2 are in the same range as FH after the metal HIR doping, with r_1 remaining practically unchanged and r_2 with a mean increase of 6.43 $s^{-1}.mM^{-1}$ which was an 11% average change in r_2 compared to naïve FH. These results confirm that the HIR process does not largely alter the physical, chemical, and magnetic properties of the FH NPs.

Radioactive Metal-FHs

Both SEC and TLC were employed for the evaluation of the HIR radiolabeling yield (RCY) and product purity (RCP). Figure 3A and B ($[^{90}Y]$Y-FH and $[^{177}Lu]$Lu-FH), and Figure 3C and D ($[^{64}Cu]$Cu-FH) present the decay corrected SEC chromatograms for generating the RCY and RCP listed in Table 3. Both RCY and RCP results were further confirmed with radio-TLC measurements (Figure S4 and Figure 3E and F) (($[^{90}Y]$Y-FH and $[^{177}Lu]$Lu-FH), and Figure 3G and H ($[^{64}Cu]$Cu-FH)), in which the radio-DFO complexes for [-^{177}Lu]Lu-DFO, $[^{90}Y]$Y-DFO and $[^{64}Cu]$Cu-DFO remained at the origin (R_f = 0.0) and radio-FHs ($[^{90}Y]$Y-FH, $[^{177}Lu]$Lu-FH and $[^{64}Cu]$Cu-FH) were moved to the solvent front (R_f ≈ 1.0) since the HIR-FH NPs were still highly negatively charged because of the CMD coating and would have insufficient retention on the cation exchange TLC plates.

For $[^{90}Y]$Y-FH, the average RCY (n = 3) was 94 ± 0.8% with RCP of 97.5 ± 1% (Table 3 and Figure 3). For $[^{177}Lu]$Lu-FH, the average RCY (n = 3) was 91 ± 0.7% with RCP of ≈ 95 ± 0.7% (Table 3 and Figure 3). For $[^{64}Cu]$Cu-FH, the average (n = 3) RCY and RCP are also listed in Table 3 and

Figure 3. The highest RCY was achieved by HV-HRR-HIR, ≈ 87.2 ± 1.2%. Results were further confirmed by the radio-TLC measurement (Figure 3G and H). The HIR synthesis of [^{64}Cu]Cu-FH using the magnetic stirrer, however, resulted in lower RCY (ie, 68.0 ± 1.1%) which is consistent with our previous study[26,27] for [^{64}Cu]Cu-FH RCY measurements and is in agreement with the yield of the nonradioactive Cu HIR condition FH incorporation indicated above (Table 1 and Figure 1C). A small percentage of the [^{64}Cu]Cu-FH NP attachments to the stirrer bar might be another reason for the lower RCY (see Figure S5). Overall, HRR-HIR technique increased the RCY by approximately 22%.

Discussion

Using our chelate-free, Heat Induced Radiolabeling (HIR) method, we show that a wide range metals, including those with radioactive isotopologues used for diagnostic imaging and radionuclide therapy, bind to the Feraheme (FH) nanoparticle (NP), a drug approved for the treatment of iron anemia. Cations with f-orbital electrons, more empty d-orbitals, larger radii, and higher positive charges achieved higher values of RCY and RCP in the HIR reaction. HIR has been further modified for syntheses of therapeutically significant [^{90}Y]Y-FH and [^{177}Lu]Lu-FH and shorter half-life [^{64}Cu]Cu-FH with high RCY and RCP.

Rational for Selection of Nonradioactive Metals

Based on the previous success of the HIR reaction both with elemental cations and element oxide form,[26–29,43,46,50] this study succeeded in extension of the HIR technique to other metals. The principle for the selection of metals was according to: 1) their radioactive isotopes are significant regarding their potentials for either radionuclide therapy ([^{89}Sr]Sr, [^{223}Ra]Ra, [^{213}Bi]Bi, [^{67}Cu]Cu, [^{149}Tb]Tb, [^{211}Pb]Pb, [^{90}Y]Y, [^{177}Lu]Lu) or biomedical imaging ([^{64}Cu]Cu) or both [^{111}In]In), and 2) their electron shell structures across the periodic table including: s-block (Sr and Ba); p-block (In, Pb, and Bi); d-block (Cu, Mo, and Y); and f-block (Sm, Eu, Tb, and Lu).

Factors Affecting HIR Efficiency (RCY) and Affinity Between Metals and FH

The Chemical Properties of Cations Play Critical Roles Affecting HIR Efficiency (RCY) and Metal/FH Affinity

Our HIR nonradioactive metal-FH results indicate that the binding affinity of a metal to FH NPs via HIR varied depending on the elements' chemical properties, charges, and radii (Table 1 and Figure 1C). In general, elements with more complete electron configuration, such as s-block ([Kr] for Sr^{2+}, [Xe] for Ba^{2+}) and d-block ([Ar]$3d^9$ for Cu^{2+}) and lower charge (Sr^{2+}, Ba^{2+}, Cu^{2+}, Pb^{2+}), were relatively less efficient for HIR reaction. However, elements with f-electrons ([Xe]$6s^24f^5$ for Sm^{3+}, [Xe]$6s^24f^4$ for Eu^{3+}, [Xe]$6s^24f^6$ for Tb^{3+}, [Xe] $6s^2$ $4f^{12}$ for Lu^{3+}), emptier d-orbitals ([Kr]4d ° for Y^{3+} vs [Kr]$4d^3$ for Mo^{3+}), larger radii (Cu vs Y and all f-block elements), and more positive charges (Pb^{2+} vs Bi^{3+}) were ideal for HIR reactions by achieving high incorporation yields (Table 1 and Figure 1C) and more stable binding (Table 2 and Figure 2B). The radiochemical analyses also demonstrated that under HIR conditions, more positively charged [^{90}Y]Y^{3+} and [^{177}Lu]Lu^{3+} reacted thermally with FH and resulted in higher RCY ([^{90}Y]Y-FH: 94±0.8%; [^{177}Lu]Lu-FH: 91±0.7%) than less positively charged [^{64}Cu]Cu^{2+} (68±1.1%) (Table 3 and Figure 3). Thus, one of the aspects of the HIR mechanism could be described as follows: the iron oxide core surface has a negative charge potential in a basic environment, which is mainly due to the dissociation of protons from hydroxyl groups of "Fe–OH" and formation of "Fe–O" at the FH core (SPION) surface.[51] Therefore, metal cations are prone to be attracted by the unshared electron pairs of Fe–O^-. Since the ionic bond energy of metal ions with a negatively charged surface is directly proportional to their charge and inversely proportional to their internuclear distance according to Coulomb's law.[52] Therefore, metal atoms with larger radii and higher oxidation state would more readily result in smaller internuclear distance, stronger electrostatic interaction, tighter binding (Table 2 and Figure 2A and B), and hence, higher radiochemical yield (RCY) (Table 1 and Figure 3).

Heat is Mandatory for HIR Higher Efficiency and Tighter Binding

In addition to the nature of the elements discussed above, heating is another driving force for the success of HIR. Metal doping takes place on the surface of iron oxide core, which has been directly supported by Temperature-dependent X-band ESR (Electron Spin Resonance) study of nonradioactive Cu-FH NP[26] and indirectly suggested by the success for [^{89}Zr]Zr^{4+} HIR of Molday ION NPs featuring at lack of CMD coating[26] and also by [^{89}Zr]Zr^{4+} and [^{111}In]In^{3+} HIR of bare $Y_3Fe_5O_{12}$ NPs.[46] Both of our previous studies[27,29] and present work demonstrate that the electrostatic interaction at room temperature is insufficient for achieving high efficiency and tight metal binding,

as is evidenced by low doping yield (Table 1 and Figure 1C) and readiness for washing off (Table 2 and Figure 2A). Conversely, a heating process is able to enhance cation diffusion through the porous CMD coating onto the core and increase the interaction energy for tighter binding attested by the higher retention of cations in FH after buffer wash (Table 2 and Figure 2B). The doping yield is also increased (Table 1, Figure 1C). The statistical analysis of the metal cation incorporation percentage (%) (HIR versus RT by a Welch's *T*-test with FDR control) indicates that heating results in a highly significant ($p \leq 0.0324$) for all but 2 metals, yielding a 4-fold increase.

Stability of Metal-FH NPs Synthesized Under HIR Condition

One of the key characters of FH NPs is its high heat stability. The typical temperature employed by HIR is 120°C, below the terminal sterilization (121°C) of the FH NP manufacture.[53] This study presents the stability by the minimal alterations of the metal-FH NPs' physical properties such as the particle sizes and relaxivities (r_1 and r_2). The sizes have a mean increase of 7.38 nm (diameter) (Table 2, Figure 2C), the r_1 values remain almost unchanged from FH, while r_2 values show a small but significant mean increase of 6.43 $s^{-1}.mM^{-1}$ (Table 2, Figure 2D). These relaxometric changes are mainly due to the use of high concentration of metals for HIR process. Most of the metals used in these studies (eg, Tb, Eu, Sm, Y, Lu, Sr, Mo and Ba)[54–62] are strong paramagnetic and hence at these concentrations may affect both r_1 and r_2 measurements. However, in the case of radiolabelled FH NP for clinical diagnostic imaging, the concentration of the radiometal is usually in nano or even pico-M (eg, for labeling 92.5 MBq of ^{89}Zr, $m_{Zr} \approx 6.25$ pM).

Our previous studies have demonstrated the radiochemical stability of HIR-FH NPs in buffer, serum and in vivo.[27,29] The PET imaging demonstrated the in vivo stability of HIR generated materials evidenced by the lack of bone activity uptake of healthy,[27] paw inflamed,[29] and wounded[43] rodent animals, which would be expected with free ^{89}Zr in vivo. In this study, we investigated the stabilities of the incorporated metals by a buffer washing method with centrifugation (Table 2 and Figure 2A and B). As indicated in Figure 2B, the metal cations are tightly bound to the FH NPs when the HIR condition was applied. A paired *T*-test was performed to compare the percentage of pre-wash metal that was retrained after a buffer wash with nanoparticles produced either with RT or HIR heating. We found a highly significant ($p<0.01E-6$) difference in metal retention: 47% for RT and 82% for heating.

Bremsstrahlung-Based Analysis of Nongamma Emitters

A bremsstrahlung-based technique has been developed for radiochemistry analysis of beta-emitters and alpha-emitters. The method was validated by correlating the activity of each five $[^{90}Y]YCl_3$ samples with 30 MBq activity against the $[^{90}Y]$Y-FH product. The ratio between the average measured activity (ie, 30 MBq) of $[^{90}Y]YCl_3$ samples and the $[^{90}Y]$Y-FH products was ≈ 95%. This was consistent with the measured RCY (94±0.8%) from the volume elution activity and radio-TLC measurements. This technique can be a general method for future HIR experiments involving beta- or alpha-emitting isotopes.

Strategies for Improving Labeling Yield (RCY) and Specific Activity (A_s)

There is a distinct A_s requirement for therapeutic applications as opposed to imaging. Imaging only requires trace quantity of activity. However, high A_s is critical for therapeutics, where treatment planning is required to ensure sufficient radiation dose is delivered to a tumor in a target organ. For this reason:

First, We Increased the Initial Amount of Activity

For yttrium-90 HIR, the amount of initial activity was increased from 18 MBq/1 mg Fe (which was the initial activity used for FH HIR with zirconium-89 in our previous study[26]) to 30 MBq/1mg Fe to escalate the loading capacity. In addition, the results presented in Tables 1 and 3 (for both the HIR nonradioactive metal-FH and radioactive metal-FH NPs) have shown that we can significantly scale the A_s by several orders of magnitude. Even though the clinical iron (Fe) dose could be as high as 5–7 mg/kg for iron-deficiency anemia treatment, for cancer radiation therapy, a lower FH iron dose and high A_s are preferred. Additionally, this is an important factor for radiolabeling short half-life isotopes (eg, copper-64). Increasing the initial activity can provide a higher metal ion (eg, copper-64) to FH nanoparticle ratio and also provides suitable timing for workflow logistics (ie, isotope delivery). The reaction rate for different initial activity and reaction time was calculated for HRR-HIR ($A_0 \approx 22$ MBq with 1 hr) and HIR ($A_0 \approx 18$ MBq with 2 hrs). This analytical calculation according to Equation 1 predicted

that by increasing A_0 from 18 MBq to 22 MBq and decreasing the reaction time from 2 hrs to 1 hr, the initial reaction rate increases by 19% (step by step calculation: see "Supplemental Material"), which is consistent with the experimental measurements for the HRR-HIR technique that increased the RCY by approximately 22%.

Second, a Heating Vortex Technique Was Developed for Mixing the Reaction Mixture

The use of a magnetic stirrer bar can cause heterogeneous mixing (FH and radioisotope ions) within the reaction volume, which may affect the RCY and cause micro-scale heterogeneous activity distribution within the labeled FH NPs. As the magnetite core of FH is superparamagnetic, a magnetic stirrer bar can have an impact on the reaction mixture, causing FH NPs to be more closely packed around the bar. Therefore, the magnetic stirrer bar was replaced with a heating vortex (HV) technique that was developed by assembling an orbital shaker with a silicon oil bath heater (Figure S1). This technique has been applied to the yttrium-90, lutetium-177 and copper-64 radiolabeling procedures. A clear distinction could be found by the [^{64}Cu]Cu-FH RCYs of HIR (68.0 ± 1.1%) vs HV-HRR-HIR (87.2 ± 1.2%) (Table 3). Furthermore, this technique would be advantageous for preparing large volumes of radiolabeled products (eg, >5mL) when agitation is more critical for generating a homogeneous reaction mixture.

Third, We Reduce Reaction Time for Short Half-Life Isotopes

Isotopes with relatively shorter half-life will quickly decay to a daughter atom that has different chemical properties, which can eventually become a competitor in the HIR process. During the reaction, in addition to activity loss, a percentage of available radiometal ions for binding to the FH NPs will be lost as well. For example, during a 2 hr HIR reaction time, the initial activity of copper-64 (half-life ≈ 13 hrs) will be reduced by approximately 15%. This reduction of available [^{64}Cu]Cu^{2+} coming either from decay to nonradioactive nickel-64 (from electron capture (43.8%) or positron (17.8%) decay paths) or zinc-64 (from beta (38.4%) decay path),[63] both of which could eventually compete with the un-decayed [^{64}Cu]Cu^{2+} for FH labeling. This results in less available [^{64}Cu]Cu^{2+} to bind with FH NPs, resulting in relatively smaller RCY (eg, 66 ± 6%[26]). Therefore, decreasing the reaction time and using higher initial activity for short half-life isotopes can improve the RCY. As we have shown in this study (Table 3) the highest RCY and RCP for [^{64}Cu]Cu-FH were achieved (≈ 87% and 99%, respectively) by applying the HV-HRR-HIR technique. These results demonstrate that the HIR protocol can be modified and optimized to achieve higher RCY and RCP for short half-life radioisotopes with a lower oxidation state (eg, [^{64}Cu]Cu^{2+}).

In summary for [^{64}Cu]Cu-FH HIR, there are three main factors in optimizing and enhancing the RCY in [^{64}Cu]Cu-FH HIR. (1) The radioisotope's half-life: The relatively short half-life of copper-64 places a constraint on the available number of copper-64 atoms per NP during the reaction time. However, by increasing the initial activity, the initial reaction rate can be increased. (2) Reaction time and temperature: Decreasing the reaction time (from 2 hrs to 1 hr) and increasing the heating temperature (from 120° C to 140°C) can also enhance the reaction rate. Decreasing the reaction time also minimizes the loss of copper-64 atoms during the reaction. (3) Mixing method: Our HV technique can replace magnetic stirring to avoid inhomogeneous mixing of SPIONs and thereby enhance the RCY. Although in this study we only performed HIR of [^{64}Cu]Cu-FH, copper-67 has similar chemistry to copper-64; thus, similar RCY and RCP are expected for [^{67}Cu]Cu-FH HIR.

Significance of Chelate-Free HIR Radiolabeling

A chelator-free FH for both therapeutic and diagnostic nano-platform may potentially enhance the performance and stability of the radio-agent in vivo. There are two major physical processes that can affect the stability of chelate-based radio–agents: bond rupture and recoil effect.[64] Both of these processes result from nuclear decay of the radiolabeled isotope. Radioisotope decay that involves the production of isomeric daughter nuclides (with excited nucleus) results in internal conversion (following γ emission from nuclear de-excitation) that consequently leads to ejecting an inner electron (from K or M shells). Similarly, radioisotopes decaying via the electron capture process can self-ionize their daughter atom by removing an electron from the inner atomic shells (eg, absorption of K shell electron by nuclear proton). Both of these processes initiate an Auger cascade leaving the atom in a highly charged state that can break the chemical bond between a chelator and the radiolabeled isotope. A recent study has shown that this bond rupture effect is responsible for breaking and freeing [^{177}Lu]Lu^{3+} from

the [^{177m}Lu]LuDOTATATE chelator.[64] Additionally, each nuclear decay event can also rupture chemical bonds in neighboring radiolabeled isotopes and result in freeing them from the chelator or nanoparticle.[65] This phenomenon may be of more concern for therapeutic constructs (with long decay chain, eg, Radium-223) since the isotopes are more capable of rupturing chemical bonds nearby.

Chelate-free radiolabeling has advanced the syntheses of multifunctional nanomaterials for biomedical applications. In contrast to the reported methods, using various platforms (eg, SiO2, iron oxide, etc.) and radioisotopes as published and reviewed previously,[36,66–75] HIR, (1) is based on a Radiometal Surface Adsorption (RSA) method[29] in which radiocations bind to the iron oxide surface of the FH NP. It uses an approved drug as the scaffold with a well-known safety profile, porous polymer coating, and high heat stability. Thus far, HIR is the only chelator-free radiolabeling method taking an approved drug as the scaffold. (2) In general, most of reported chelate-free methods are designed specifically for a single isotope.[36,50] HIR, however, provides a nano-platform able to incorporate a wide range of therapeutic and diagnostic cations such as yttrium-90, lutetium-177, indium-111, copper-64, lead, and bismuth, as proved by this work (Figures 1C and 2) and our previous studies.[26,27,29] (3) HIR might be potentially significant for radiolabeling of therapeutically important alpha emitters. Since they have long decay chains (such as ^{223}Ra, ^{225}Ac, ^{211}At, ^{213}Bi, ^{209}Pb),[76,77] the HIR method might be capable of retaining both the parent and daughter radionuclides since HIR bypasses the strict geometric requirements for chelation chemistry. (4) Moreover, our recent study[28] has demonstrated that a targeted radiolabeled FH can be developed by utilizing the click chemistry to attach bioactive groups to the surface of HIR FH NPs. Thus, HIR-FH can also potentially offer a unique platform for targeted and selective internal radionuclide therapy,[78] while HIR-FH or in general any HIR radiometal-SPION can serve as metal-based radio-enhancer as we have recently reported.[79] With its simple chemical synthesis procedure, HIR can be potentially utilized in clinical settings without the possible complications of a chelate-based chemistry.[33–35,46,50] (5) While there currently exist both single-[72] or dual-modality[66] nanoparticle platforms, the chelate-free HIR method discussed in this work is also conducive to the development of multimodal imaging probes, allowing for new areas of research. Specifically, HIR generated radioactive FH NPs offer multimodal imaging such as PET[27,29,43] and MRI[22–25] and the simultaneous MRI would be leveraged with HIR radiometal-FH nano-platform for three-dimensional radiation dosimetry studies, an area with important clinical significance.[80]

Conclusion

As noted, FH is a drug consisting of an iron oxide core surrounded by CMD. The CMD coating is heat stable, surviving both terminal sterilization during manufacture and the temperatures of the HIR reactions, with little or no change in nanoparticle size and relaxivity. The CMD coating is cation porous, exposing the iron oxide to hydrogen ions that lead to iron oxide dissolution in phagolysosomes, and allowing access for cations that bind to the iron oxide surface in the HIR reaction. Thus, the CMD-iron oxide bond of FH survives heat stresses but is cation porous, a combination of properties that, as far as we are aware, is unique to FH. The present study demonstrates that the chelate-free HIR technique can be extended to a range of clinically relevant therapeutic isotopes. Metal cations with f-electrons, more empty d-orbitals, larger radii and more positive charges are more effective for HIR reactions by achieving high RCY and RCP. The HIR technique could be further technically optimized for higher RCY by enhancing the reaction rate and utilizing a heating vortex system for short half-life isotopes (eg, [^{64}Cu]Cu^{2+}). HIR-FH nanoparticles with therapeutic potential ([^{90}Y]Y-FH and [^{177}Lu]Lu-FH) could be synthesized with both high RCY and RCP. Thus, this study extends the HIR technique to a general approach for generating therapeutically and diagnostically significant nanoconstructs.

Abbreviations

A_0, initial activity; A_s, specific activity; CMD, carboxymethyldextran; CTW, chelex-treated water; DFO, deferoxamine mesylate salt; DLS, dynamic light scattering; DTPA, diethylenetriaminepentaacetic acid; EDTA, ethylenediaminetetraacetic acid; FH, Feraheme (Ferumoxytol); FDR, false discovery rate; g, g-force; HEPES, (4-(2-hydroxyethyl)-1-piperazineethanesulfonic acid); HIR, heat-induced radiolabeling; HRR-HIR, higher reaction rate-HIR; HV, heating vortex; HV-HRR-HIR, higher reaction rate HIR under heating vortex; ICP-MS, inductively coupled plasma mass spectrometry; MRI, magnetic resonance imaging; NMRS, nuclear magnetic relaxation spectrometry; NP, nanoparticle; PET, positron emission tomography; PK, pharmacokinetics'; r_1 & r_2, transverse (r_1, spin-lattice) and longitudinal (r_2, spin-spin) relaxivities; RCY, radiochemical yield;

RCP, radiochemical purity; RCF, relative centrifugal force; R_f, rate of flow value of TLC; RT, room temperature; RSA, Radiocation Surface Adsorption; SEC, size exclusion chromatography; SPION, superparamagnetic iron oxide nanopartcles; TLC, thin layer chromatography.

Acknowledgments

This work was partially supported by the Sydney Vital Clinical Translation Cancer Research Centre, the Kolling Institute of Medical Research, the University of Sydney and USA National Institute of Health (NIH): P41EB022544, S10OD010650, T32HL007208, 1R01EB017699-01, CaNCURE award: R25CA174650. We also would like to acknowledge Professor Dale Bailey from the Royal North Shore Hospital for providing the ^{90}Y and ^{177}Lu isotopes.

Disclosure

The author reports no conflicts of interest in this work.

References

1. Assadi M, Afrasiabi K, Nabipour I, Seyedabadi M. Nanotechnology and nuclear medicine; research and preclinical applications. *Hell J Nucl Med*. 2011;14:149–159.
2. Chakravarty R, Goel S, Dash A, Cai W. Radiolabeled inorganic nanoparticles for positron emission tomography imaging of cancer: an overview. *Q J Nucl Med Mol Imaging*. 2017;61:181–204. doi:10.23736/s1824-4785.17.02969-7
3. Farrag NS, El-Sabagh HA, Al-mahallawi AM, et al. Comparative study on radiolabeling and biodistribution of core-shell silver/polymeric nanoparticles-based theranostics for tumor targeting. *Int J Pharm*. 2017;529:123–133. doi:10.1016/j.ijpharm.2017.06.044
4. Farzin L, Sheibani S, Moassesi ME, Shamsipur M. An overview of nanoscale radionuclides and radiolabeled nanomaterials commonly used for nuclear molecular imaging and therapeutic functions. *J Biomed Mater Res*. 2019;107:251–285. doi:10.1002/jbm.a.36550
5. Goel S, England CG, Chen F, Cai W. Positron emission tomography and nanotechnology: A dynamic duo for cancer theranostics. *Adv Drug Deliv Rev*. 2017;113:157–176. doi:10.1016/j.addr.2016.08.001
6. Jiang X, Han Y, Zhang H, et al. Cu-Fe-Se ternary nanosheet-based drug delivery carrier for multimodal imaging and combined chemo/photothermal therapy of cancer. *ACS Appl Mater Interfaces*. 2018;10:43396–43404. doi:10.1021/acsami.8b15064
7. Koziorowski J, Stanciu AE, Gomez-Vallejo V, Llop J. Radiolabeled nanoparticles for cancer diagnosis and therapy. *Anticancer Agents Med Chem*. 2017;17:333–354. doi:10.2174/1871520616666160219162902
8.. Pant K, Sedlacek O, Nadar RA, Hruby M, Stephan H. Radiolabelled polymeric materials for imaging and treatment of cancer: quo vadis? *Adv Healthc Mater*. 2017;6. doi:10.1002/adhm.201601115
9. Polyak A, Ross TL. Nanoparticles for SPECT and PET imaging: towards personalized medicine and theranostics. *Curr Med Chem*. 2018;25:4328–4353. doi:10.2174/0929867324666170830095553
10. Zhao L, Zhu M, Li Y, Xing Y, Zhao J. Radiolabeled dendrimers for nuclear medicine applications. *Molecules*. 2017;22:1350. doi:10.3390/molecules22091350
11. Fallahpoor M, Abbasi M, Parach AA, Kalantari F. Internal dosimetry for radioembolization therapy with Yttrium-90 microspheres. *J Appl Clin Med Phys*. 2017;18:176–180. doi:10.1002/acm2.12042
12. Gulec SA. Y-90 radiomicrosphere therapy for colorectal cancer liver metastases. *Semin Nucl Med*. 2016;46:126–134. doi:10.1053/j.semnuclmed.2015.10.008
13. Kim D-H, Li W, Chen J, et al. Multimodal imaging of nanocomposite microspheres for transcatheter intra-arterial drug delivery to liver tumors. *Sci Rep*. 2016;6:29653. doi:10.1038/srep29653
14. Mahnken AH. (90)Y-glass microspheres for hepatic neoplasia. *Future Oncol*. 2015;11:1343–1354. doi:10.2217/fon.15.12
15. Wang EA, Stein JP, Bellavia RJ, Broadwell SR. Treatment options for unresectable HCC with a focus on SIRT with Yttrium-90 resin microspheres. *Int J Clin Pract*. 2017;71:e12972. doi:10.1111/ijcp.12972
16. Bradbury MS, Pauliah M, Zanzonico P, Wiesner U, Patel S. Intraoperative mapping of sentinel lymph node metastases using a clinically translated ultrasmall silica nanoparticle. *Wiley Interdiscip Rev Nanomed Nanobiotechnol*. 2016;8:535–553. doi:10.1002/wnan.1380
17. Bradbury MS, Phillips E, Montero PH, et al. Clinically-translated silica nanoparticles as dual-modality cancer-targeted probes for image-guided surgery and interventions. *Integr Biol (Camb)*. 2013;5:74–86. doi:10.1039/c2ib20174g
18. Faries MB, Bedrosian I, Reynolds C, et al. Active macromolecule uptake by lymph node antigen-presenting cells: a novel mechanism in determining sentinel lymph node status. *Ann Surg Oncol*. 2000;7:98–105. doi:10.1007/s10434-000-0098-6
19. Krag D, Weaver D, Ashikaga T. et al. The sentinel node in breast cancer–a multicenter validation study. *N Engl J Med*. 1998;339:941–946. doi:10.1056/nejm199810013391401
20. Olmos RA, Vidal-Sicart S, Nieweg OE. SPECT-CT and real-time intraoperative imaging: new tools for sentinel node localization and radioguided surgery? *Eur J Nucl Med Mol Imaging*. 2009;36:1–5. doi:10.1007/s00259-008-0955-2
21. Wilhelm AJ, Mijnhout GS, Franssen EJ. Radiopharmaceuticals in sentinel lymph-node detection - an overview. *Eur J Nucl Med*. 1999;26:S36–S42. doi:10.1007/pl00014793
22. Bashir MR, Bhatti L, Marin D, Nelson RC. Emerging applications for ferumoxytol as a contrast agent in MRI. *J Magn Reson Imaging*. 2015;41:884–898. doi:10.1002/jmri.24691
23. Farrell BT, Hamilton BE, Dosa E, et al. Using iron oxide nanoparticles to diagnose CNS inflammatory diseases and PCNSL. *Neurology*. 2013;81:256–263. doi:10.1212/WNL.0b013e31829bfd8f
24. Hamilton BE, Nesbit GM, Dosa E, et al. Comparative analysis of ferumoxytol and gadoteridol enhancement using T1- and T2-weighted MRI in neuroimaging. *AJR Am J Roentgenol*. 2011;197:981–988. doi:10.2214/ajr.10.5992
25. McCullough BJ, Kolokythas O, Maki JH, Green DE. Ferumoxytol in clinical practice: implications for MRI. *J Magn Reson Imaging*. 2013;37:1476–1479. doi:10.1002/jmri.23879
26. Boros E, Bowen AM, Josephson L, Vasdev N, Holland JP. Chelate-free metal ion binding and heat-induced radiolabeling of iron oxide nanoparticles. *Chem Sci*. 2015;6:225–236. doi:10.1039/c4sc02778g
27. Normandin MD, Yuan H, Wilks MQ, et al. Heat-induced radiolabeling of nanoparticles for monocyte tracking by PET. *Angew Chem Int Ed Engl*. 2015;54:13002–13006. doi:10.1002/anie.201505525
28. Yuan H, Wilks MQ, El Fakhri G, et al. Heat-induced-radiolabeling and click chemistry: A powerful combination for generating multifunctional nanomaterials. *PLoS One*. 2017;12:e0172722. doi:10.1371/journal.pone.0172722
29. Yuan H, Wilks MQ, Normandin MD, et al. Heat-induced radiolabeling and fluorescence labeling of Feraheme nanoparticles for PET/SPECT imaging and flow cytometry. *Nat Protoc*. 2018;13:392–412. doi:10.1038/nprot.2017.133

30. Keliher EJ, Yoo J, Nahrendorf M, et al. 89Zr-labeled dextran nanoparticles allow in vivo macrophage imaging. *Bioconjug Chem*. 2011;22:2383–2389. doi:10.1021/bc200405d
31. Thorek DLJ, Ulmert D, Diop N-FM, et al. Non-invasive mapping of deep-tissue lymph nodes in live animals using a multimodal PET/MRI nanoparticle. *Nat Commun*. 2014;5:3097. doi:10.1038/ncomms4097
32. Wunderbaldinger P, Josephson L, Bremer C, Moore A, Weissleder R. Detection of lymph node metastases by contrast-enhanced MRI in an experimental model. *Magn Reson Med*. 2002;47:292–297. doi:10.1002/(ISSN)1522-2594
33. Cutler CS, Hennkens HM, Sisay N, Huclier-Markai S, Jurisson SS. Radiometals for combined imaging and therapy. *Chem Rev*. 2013;113:858–883. doi:10.1021/cr3003104
34. Liu S. Bifunctional coupling agents for radiolabeling of biomolecules and target-specific delivery of metallic radionuclides. *Adv Drug Deliv Rev*. 2008;60:1347–1370. doi:10.1016/j.addr.2008.04.006
35. Price EW, Orvig C. Matching chelators to radiometals for radiopharmaceuticals. *Chem Soc Rev*. 2014;43:260–290. doi:10.1039/c3cs60304k
36. Goel S, Chen F, Ehlerding EB, Cai W. Intrinsically radiolabeled nanoparticles: an emerging paradigm. *Small*. 2014;10:3825–3830. doi:10.1002/smll.201401048
37. Liu K-X, Lan F, Jiang W, et al. Controllable preparation of ternary superparamagnetic nanoparticles dual-doped with Mn and Zn elements. *J Nanosci Nanotechnol*. 2012;12:8437–8442. doi:10.1166/jnn.2012.6672
38. Weissleder R, Stark DD, Engelstad BL, et al. Superparamagnetic iron oxide: pharmacokinetics and toxicity. *AJR Am J Roentgenol*. 1989;152:167–173. doi:10.2214/ajr.152.1.167
39. Wong RM, Gilbert DA, Liu K, Louie AY. Rapid size-controlled synthesis of dextran-coated, 64Cu-doped iron oxide nanoparticles. *ACS Nano*. 2012;6:3461–3467. doi:10.1021/nn300494k
40. Freund B, Tromsdorf UI, Bruns OT, et al. A simple and widely applicable method to 59Fe-radiolabel monodisperse superparamagnetic iron oxide nanoparticles for in vivo quantification studies. *ACS Nano*. 2012;6:7318–7325. doi:10.1021/nn3024267
41. Israel LL, Karimi F, Bianchessi S, et al. Surface metal cation doping of maghemite nanoparticles: modulation of MRI relaxivity features and chelator-free 68 Ga-radiolabelling for dual MRI-PET imaging. *Mater Res Express*. 2015;2:095009. doi:10.1088/2053-1591/2/9/095009
42. Shi S, Xu C, Yang K, et al. Chelator-Free Radiolabeling of Nanographene: breaking the Stereotype of Chelation. *Angew Chem Int Ed Engl*. 2017;56:2889–2892. doi:10.1002/anie.201610649
43. Sirbulescu RF, Boehm CK, Soon E, et al. Mature B cells accelerate wound healing after acute and chronic diabetic skin lesions. *Wound Repair Regener*. 2017;25:774–791. doi:10.1111/wrr.12584
44. Gholami YH, Willowson KP, Forwood NJ, et al. Comparison of radiobiological parameters for (90)Y radionuclide therapy (RNT) and external beam radiotherapy (EBRT) in vitro. *EJNMMI Phys*. 2018;5:18. doi:10.1186/s40658-018-0217-8
45. Wright CL, Zhang J, Tweedle MF, Knopp MV, Hall NC. Theranostic Imaging of Yttrium-90. *Biomed Res Int*. 2015;2015:481279. doi:10.1155/2015/481279
46. Patrick PS, Bogart LK, Macdonald TJ, et al. Surface radio-mineralisation mediates chelate-free radiolabelling of iron oxide nanoparticles. *Chem Sci*. 2019;10:2592–2597. doi:10.1039/c8sc04895a
47. Bullivant JP, Zhao S, Willenberg B, et al. Materials characterization of Feraheme/ferumoxytol and preliminary evaluation of its potential for magnetic fluid hyperthermia. *Int J Mol Sci*. 2013;14:17501–17510. doi:10.3390/ijms140917501
48. Pohlmann A, Karczewski P, Ku MC, et al. Cerebral blood volume estimation by ferumoxytol-enhanced steady-state MRI at 9.4 T reveals microvascular impact of alpha1 -adrenergic receptor antibodies. *NMR Biomed*. 2014;27:1085–1093. doi:10.1002/nbm.3160
49. Ramanathan RK, Korn RL, Raghunand N, et al. Correlation between ferumoxytol uptake in tumor lesions by MRI and response to nanoliposomal irinotecan in patients with advanced solid tumors: a pilot study. *Clin Cancer Res*. 2017;23:3638–3648. doi:10.1158/1078-0432.ccr-16-1990
50. Lamb J, Holland JP. Advanced methods for radiolabeling multimodality nanomedicines for SPECT/MRI and PET/MRI. *J Nucl Med*. 2018;59:382–389. doi:10.2967/jnumed.116.187419
51. Yu SC, Chow GM. Carboxyl group (–CO2H) functionalized ferrimagnetic iron oxide nanoparticles for potential bio-applications. *J Mater Chem*. 2004;14:2781–2786. doi:10.1039/B404964K
52. Okumura H, Itoh SG, Okamoto Y. *Generalized-Ensemble Algorithms for Simulations of Complex Molecular Systems. In Practical Aspects of Computational Chemistry II: An Overview of the Last Two Decades and Current Trends*. Netherlands: Springer; 2012:69–101.
53. Groman EV, Paul KG, Frigo TB, Bengele H, Lewis JM Heat stable colloidal iron oxides coated with reduced carbohydrates and derivatives. US patent, US6599498. 2003.
54. Aizawa SI, Okano M, Kidani T. Enantiomeric NMR signal separation behavior and mechanism of samarium(III) and neodymium(III) complexes with (S,S)-ethylenediamine-N,N'-disuccinate. *Chirality*. 2017;29:273–281. doi:10.1002/chir.22681
55. Gustafsson HA, Söderlind M, Córdoba Gallego JM, et al. Magnetic and electron spin relaxation properties of (Gdxy1−x)2o3 ($0 \leq x \leq 1$) nanoparticles synthesized by the combustion method. increased electron spin relaxation times with increasing yttrium content. *J Phys Chem*. 2011;C 115:5469–5477.
56. Han G, Deng Y, Sun J, Ling J, Shen Z. Research into europium complexes as magnetic resonance imaging contrast agents (Review). *Exp Ther Med*. 2015;9:1561–1566. doi:10.3892/etm.2015.2297
57. Marti-Bonmati L, Vilar J, Paniagua JC, Talens A. High density barium sulphate as an MRI oral contrast. *Magn Reson Imaging*. 1991;9:259–261. doi:10.1016/0730-725x(91)90019-i
58. Vuong QL, Van Doorslaer S, Bridot J-L, et al. Paramagnetic nanoparticles as potential MRI contrast agents: characterization, NMR relaxation, simulations and theory. *MAGMA*. 2012;25:467–478. doi:10.1007/s10334-012-0326-7
59. Williams HM. The application of magnetic nanoparticles in the treatment and monitoring of cancer and infectious diseases. *Biosci Horiz*. 2017;10.
60. Xu W, Kattel K, Park JY, et al. Paramagnetic nanoparticle T1 and T2 MRI contrast agents. *Phys Chem Chem Phys*. 2012;14:12687–12700. doi:10.1039/c2cp41357d
61. Yu YC, Lin LP, Yang Z, et al. Microwave-assisted preparation of paramagnetic zwitterionic amphiphilic copolymer hybrid molybdenum disulfide for T1-weighted magnetic resonance imaging-guided photothermal therapy. *J Mater Chem B*. 2018;6:6391–6398. doi:10.1039/C8TB01660G
62. Zairov R, Mustafina A, Shamsutdinova N, et al. High performance magneto-fluorescent nanoparticles assembled from terbium and gadolinium 1,3-diketones. *Sci Rep*. 2017;7:40486. doi:10.1038/srep40486
63. Shokeen M, Anderson CJ. Molecular imaging of cancer with copper-64 radiopharmaceuticals and positron emission tomography (PET). *Acc Chem Res*. 2009;42:832–841. doi:10.1021/ar800255q
64. Bhardwaj R, van der Meer A, Das SK, et al. Separation of nuclear isomers for cancer therapeutic radionuclides based on nuclear decay after-effects. *Sci Rep*. 2017;7:44242. doi:10.1038/srep44242
65. Welch MJ. *Radiopharmaceuticals and Other Compounds Labelled with Short-Lived Radionuclides*. Elsevier; 2013.
66. Chen F, Ellison PA, Lewis CM, et al. Chelator-free synthesis of a dual-modality PET/MRI agent. *Angew Chem Int Ed Engl*. 2013;52:13319–13323. doi:10.1002/anie.201306306
67. Chen F, Goel S, Valdovinos HF, et al. In vivo integrity and biological fate of chelator-free zirconium-89-labeled mesoporous silica nanoparticles. *ACS Nano*. 2015;9:7950–7959. doi:10.1021/acsnano.5b00526
68. Chen F, Ma K, Zhang L, et al. Target-or-clear zirconium-89 labeled silica nanoparticles for enhanced cancer-directed uptake in melanoma: a comparison of radiolabeling strategies. *Chem Mater*. 2017;29:8269–8281. doi:10.1021/acs.chemmater.7b02567

69. Cheng L, Shen S, Jiang D, et al. Chelator-free labeling of metal oxide nanostructures with zirconium-89 for positron emission tomography imaging. *ACS Nano*. 2017;11:12193–12201. doi:10.1021/acsnano.7b05428
70. Goel S, Chen F, Luan S. et al. Engineering intrinsically zirconium-89 radiolabeled self-destructing mesoporous silica nanostructures for in vivo biodistribution and tumor targeting studies. *Adv Sci*. 2016;3:1600122. doi:10.1002/advs.201600122
71. Madru R, Budassi M, Benveniste H, et al. Simultaneous preclinical positron emission tomography-magnetic resonance imaging study of lymphatic drainage of chelator-free (64)Cu-Labeled nanoparticles. *Cancer Biother Radiopharm*. 2018;33:213–220. doi:10.1089/cbr.2017.2412
72. Miller L, Winter G, Baur B, et al. Synthesis, characterization, and biodistribution of multiple 89Zr-labeled pore-expanded mesoporous silica nanoparticles for PET. *Nanoscale*. 2014;6:4928–4935. doi:10.1039/c3nr06800e
73. Shaffer TM, Wall MA, Harmsen S, et al. Silica nanoparticles as substrates for chelator-free labeling of oxophilic radioisotopes. *Nano Lett*. 2015;15:864–868. doi:10.1021/nl503522y
74. Zhan Y, Ehlerding EB, Shi S, et al. Intrinsically zirconium-89-labeled manganese oxide nanoparticles for in vivo dual-modality positron emission tomography and magnetic resonance imaging. *J Biomed Nanotechnol*. 2018;14:900–909. doi:10.1166/jbn.2018.2498
75. Zhou M, Zhang R, Huang M, et al. A chelator-free multifunctional [64Cu]CuS nanoparticle platform for simultaneous micro-PET/CT imaging and photothermal ablation therapy. *J Am Chem Soc*. 2010;132:15351–15358. doi:10.1021/ja106855m
76. Ma D, McDevitt MR, Finn RD, Scheinberg DA. Breakthrough of 225Ac and its radionuclide daughters from an 225Ac/213Bi generator: development of new methods, quantitative characterization, and implications for clinical use. *Appl Radiat Isot*. 2001;55:667–678. doi:10.1016/s0969-8043(01)00062-8
77. Morgenstern A, Bruchertseifer F, Apostolidis C. Bismuth-213 and actinium-225 – generator performance and evolving therapeutic applications of two generator-derived alpha-emitting radioisotopes. *Curr Radiopharm*. 2012;5:221–227. doi:10.2174/1874471011205030221
78. Kuncic Z, Lacombe S. Nanoparticle radio-enhancement: principles, progress and application to cancer treatment. *Phys Med Biol*. 2018;63:02TR01. doi:10.1088/1361-6560/aa99ce
79. Gholami YM, Kuncic Z, Kuncic Z. Radio-enhancement effects by radiolabeled nanoparticles. *Sci Rep*. 2019;9. doi:10.1038/s41598-019-50861-2
80. Calmet C, Bonnet J, Bertino C, Catala A, Martinez M, Joffre F. MRI dosimetry: a fast quantitative MRI method to determine 3D absorbed dose distributions. *Invest Radiol*. 1999;34:236–241.

Video abstract

Point your SmartPhone at the code above. If you have a QR code reader the video abstract will appear. Or use: https://youtu.be/_SYXGLeZuWM